RSC Advances

RSC Publishing

PAPER

View Article Online
View Journal | View Issue

Cite this: *RSC Advances*, 2013, **3**, 8517

Multifunctional $NaYF_4$:Yb/Er/Gd nanocrystal decorated SiO_2 nanotubes for anti-cancer drug delivery and dual modal imaging†

Xuejiao Li,[ab] Zhiyao Hou,*[a] Ping'an Ma,[a] Xiao Zhang,[a] Chunxia Li,[a] Ziyong Cheng,[a] Yunlu Dai,[a] Jianshe Lian[b] and Jun Lin*[a]

Silica nanotubes (SNTs) functionalized with magnetic and up-conversion luminescent (UCL) $NaYF_4$:Yb/Er/Gd nanocrystals (NCs) (denoted as MUCNCs@SNTs) have been prepared by single-nozzle electrospinning based on a phase separation effect without any templates. Monodisperse and hydrophilic cubic α-$NaYF_4$:Yb/Er/Gd NCs decorated with polyethyleneimine (PEI) were fabricated in a facile hydrothermal route. Then, the Gd^{3+}-doped α-$NaYF_4$:Yb/Er NCs were dispersed into the electrospinning precursor solution containing polyvinylpyrrolidone (PVP) and tetraethylorthosilicate (TEOS), followed by the preparation of precursor nanotubes *via* electrospinning process. Finally, after annealing at 600 °C, pure MUCNCs@SNTs were obtained. The biocompatibility test on L929 fibroblast cells using MTT assay reveals low cytotoxicity of the composites. Doxorubicin hydrochloride (DOX), a typical anti-cancer drug, was introduced into MUCNCs@SNTs to evaluate the loading and sustained release behaviours. The composite carriers provide pH-dependent drug release behaviour owing to abundant Si–OH active bonds of silica and its interactions with DOX. The *in vitro* cytotoxicity and cell uptake behaviour of the MUCNCs@SNTs for HeLa cells were evaluated. For *in vitro* magnetic resonance imaging (MRI), the composites show the promising spin lattice relaxation time (T_1) weighted effect and could potentially apply as a T_1-positive contrast agent. In addition, the composites show near-infrared UC luminescence and were successfully applied in the bioimaging of HeLa cells. Considering the good biocompatibility, high drug releasing content and pH-dependent drug release of the materials, these magnetic and luminescent composite nanotubes have potential applications in drug sustained release and magnetic resonance/UC luminescence modality imaging.

Received 27th February 2013,
Accepted 15th March 2013

DOI: 10.1039/c3ra40992a

www.rsc.org/advances

Introduction

Now much attention has been paid to novel drug-storage/release systems in the fields of modern medicine and pharmaceuticals, due to their numerous advantages over traditional forms of dosage, such as enhanced bioavailability, controlled and prolonged released time, greater efficacy and safety, and predictable therapeutic response.[1–3] Normally, an ideal drug-delivery system (DDS) should not only protect the drug from biological degradation before reaching the target organs or cells, but also provide a sustained controlled release in the physiological condition.[4–7] So far, a series of inorganic biomaterials such as hydroxyapatite (HAp),[8,9] calcium phosphate cement (CPC),[10,11] bioactive glasses,[12–14] bioceramics,[15,16] xerogels,[17] and calcium silicate[18,19] have been successfully exploited in sustained/controlled drug delivery based on their improved drug loading efficiency and degradable properties. However, the amount of drug release has been one limitation in the DDSs above. In consideration of different nanostructures of DDSs, inorganic nanotubes may solve the problem while the inner void can take up a large amount of drugs, and the open ends of pores serve as gates that can control the release of drugs.[20,21]

Among those tubular nanomaterials, silica nanotubes (SNTs) have aroused wide concern because of their hydrophilic nature, easy colloidal suspension formation, and surface functionalization accessibility for both inner and outer walls.[22–24] The general strategy for the synthesis of hollow structures is a template-assisted process which tends to be rather complicated, with the obvious drawback that the removal process often compromises the structural integrity of the final products and limits the practical applications. Therefore it is necessary and important to develop an easy and

[a]*State Key laboratory of Rare Earth Resource Utilization, Changchun Institute of Applied Chemistry, Chinese Academy of Sciences, Changchun, 130022, PR China. E-mail: jlin@ciac.jl.cn; zyhou@ciac.jl.cn*

[b]*Key Lab of Automobile Materials, Ministry of Education, College of Materials Science and Engineering, Jilin University, Changchun, 130025, PR China*

† Electronic supplementary information (ESI) available. See DOI: 10.1039/c3ra40992a

direct method to fabricate highly purified SNTs. During the past decade, the electrospinning technique has become one of the most frequently-used methods to fabricate one dimensional nanostructures at low cost.[25,26] Here, single-nozzle electrospinning based on a phase separation effect without any templates was brought up to fabricate nanotube structure. To the best of our knowledge, silica tubes functionalized with photoluminescence (PL) *via* an electrospinning process have never been really tested as DDSs to demonstrate their potential application. Self-activated SNTs show auto-fluorescence under short-wavelength ultraviolet (UV) radiation, which greatly decrease the signal-to-noise and detection sensitivity. Compared with the conventional down-conversion process, up-conversion (UC) luminescent materials have many advantages after being excited by lower-energy near-infrared (NIR) photons, such as greater tissue penetration, weak autofluorescence from cells or tissues, and high signal-to-noise ratio.[27–34] As a result, rare earth up-conversion nanophosphors accompanied with many advantages, such as the use of non-invasive NIR radiation and the absence of autofluorescence, have been applied in photoluminescence bioimaging exhibit.[35,36] However, photoluminescent imaging has one shortcoming of the low penetration depth of the excitation and emission light, and this can be solved by magnetic resonance imaging (MRI).[37,38] Therefore, the design and development of silica nanotubes functionalized with magnetic and UC luminescent properties as drug carriers are undoubtedly of great importance in the field of drug delivery and modality imaging.[39,40] Unfortunately, little attention has been paid to this area so far.[41]

As a continuation of our former research of drug storage/release,[42–45] in this paper, we intend to prepare $NaYF_4$:Yb/Er/Gd (the efficient NIR-to-visible UC material[46–49])-decorated SNTs as DDS *via* the electrospinning method. By introducing Gd^{3+} in the host matrix, magnetic and UC luminescent $NaYF_4$:Yb/Er/Gd NCs (MUCNCs) have successfully been fabricated for dual modal imaging of T_1-enhanced magnetic resonance and UC luminescence. Firstly, hydrophilic cubic α-$NaYF_4$:Yb/Er/Gd NCs decorated with PEI which could control the growth of the crystals were fabricated by a facile hydrothermal route.[50] Then, the MUCNCs were dispersed into electrospinning solution, followed by the preparation of precursor hybrid tubes containing MUCNCs *via* electrospinning process. Finally, after annealing at 600 °C, MUCNCs@SNTs were obtained. The biocompatibility test on L929 fibroblast cells using the MTT assay reveals the low cytotoxicity of the system. The obtained materials have been studied as a DDS by using doxorubicin hydrochloride (DOX) as a model drug. The drug loading and releasing properties, cytotoxicity, and cellular uptake behavior were examined in detail. Furthermore, the effectiveness of MUCNCs@SNTs composites as a multifunctional bioprobe has been demonstrated by *in vitro* magnetic resonance/UC luminescence modality imaging.

Experimental section

Chemicals and materials

Tetraethyl orthosilicate (TEOS, analytical reagent, A. R.) were purchased from Beijing Yili Fine Chemicals Co., Ltd. Polyvinylpyrrolidone (PVP, M_w = 1 300 000) and polyethyleneimine (PEI, branched polymer $(-NHCH_2CH_2-)_x(-N(CH_2CH_2NH_2)CH_2CH_2-)_y$) were purchased from Aldrich. DOX was obtained from the Nanjing Duodian Chemical Limited Company. The rare earth oxides RE_2O_3 (99.99%) (RE = Y, Yb, Er, Gd) were purchased from Science and Technology Parent Company of Changchun Institute of Applied Chemistry and other chemicals were purchased from Beijing Chemical Co., Ltd. $YbCl_3$, $ErCl_3$, $GdCl_3$ and YCl_3 crystals were prepared by dissolving corresponding oxides in hydrochloric acid and heating, then dissolved in ethylene glycol (0.5 M). All chemicals are of analytical grade reagents and used directly without further purification.

Synthesis of water-dispersible PEI coated MUCNCs

In a typical procedure for preparing $NaYF_4$ particles, 0.2 g PEI, 1.2 mmol of NaCl and 1.2 mL $RECl_3$ (0.5 M, RE: 72%Y^{3+}, 17%Yb^{3+}, 3%Er^{3+}, 8% Gd^{3+} mole ratio) were first added into 7.8 mL of ethylene glycol under vigorous stirring until forming a transparent solution. Subsequently, 3.6 mmol NH_4F was added into 9 mL ethylene glycol. After vigorous stirring for 15 min, the two solutions above were mixed together, and then transferred into a 50 mL Teflon autoclave, which was tightly sealed and maintained at 200 °C for only 1 h. As the autoclave was cooled to room temperature naturally, the NCs obtained were collected by centrifugation, washed three times with ethanol and deionized water, and finally dispersed in 5 mL H_2O.

Synthesis of magnetic and UC luminescent MUCNCs@SNTs

Magnetic and UC luminescent functionalized silica nanotubes were prepared by electrospinning using TEOS as silicon source. 2 mL TEOS was mixed with 0.1 mM PVP solution in ethanol. Then 2.5 mL of water soluble MUCNCs solution was added drop by drop under vigorous stirring. 2 h later, the mixture was transferred into a single-nozzle electrospinning setup. The distance between the spinneret (a metallic needle) and the collector (a grounded conductor) was fixed at 15 cm and the high-voltage supply was maintained at 8 kV. The spinning rate was controlled at 1.0 mL h^{-1} by a syringe pump (TJ-3AW/0109-1B, Baoding Longer Precision Pump Co., Ltd, China). The as-spun fibers were collected on the collector. After electrospinning, these precursor PVP/TEOS fibers were placed in a Petri dish and dried for more than 1 day. The as-prepared hybrid precursor samples annealed in an air atmosphere at 200 °C for 2 h and then calcined in air at 600 °C for 3 h with the heating rate of 2 °C min^{-1}. Finally, pure MUCNCs@silica hollow tubes were obtained.

The biocompatibility of the MUCNCs@SNTs

To evaluate the biocompatibility of the MUCNCs@SNTs, MTT cell assay was used on the L929 cell. MTT is a standard test for screening the toxicity of biomaterials and is carried out in accordance with ASTM standards. This method is based on the

formation of dark red formazan by the metabolically active cells after their exposure to MTT[3-(4,5-dimethylthiazol-2-yl)-2,5-diphenyltetrazolium bromide]. Briefly, plate 5000–6000 L929 fibroblast cells in 100 μL media per well in a 96 well plate. Incubate (37 °C, 5% CO_2) overnight to allow the cells to attach to the wells. The MUCNCs@SNTs were sterilized by ultraviolet irradiation for 2 h, and then serial dilutions of the nanocomposites at concentrations of 3.125, 6.25, 12.5, 25, 50, 100 and 200 μg mL^{-1} were added to the culture wells and incubated for another 24 h in 5% CO_2 at 37 °C. 5 mg mL^{-1} stock solution of MTT was prepared in PBS and this stock solution (20 μL) was added to each well containing a different amount of the monodisperse MUCNCs@SNTs. The plate was incubated at 37 °C for 4 h. During this period viable cells reduce MTT to formazan pigment, which can be dissolved by dimethyl sulfoxide (DMSO). The supernatant in each well was aspirated. After incubation, 150 μL of DMSO was added to each well, and placed on a shaking table, 150 rpm for 5 min, to thoroughly mix the formazan into the solvent. The absorbance of the suspension was recorded under a microplate reader (Thermo Multiskan mk3) at 490 nm.

Preparation of drug storage/delivery systems

10 mg of UCNCs@SNT samples dispersing in 0.5 mL water were mixed with 2 mL of DOX aqueous solution (1 mg mL^{-1}). After stirring for 24 h under dark conditions, the DOX-loaded samples were collected by centrifugation and denoted as DOX-MUCNCs@SNTs. Then, DOX-MUCNCs@SNTs were transferred to a dialysis tube and immersed in 2 mL pH = 7.4 and 5 phosphoric acidic buffer solutions (PBS) at 37 °C with gentle shaking. At predetermined time intervals, PBS was taken by centrifugation and replaced with an equal volume of fresh PBS. The amounts of released DOX in the supernatant solutions were measured by UV-vis spectrophotometer at a wavelength of 480 nm. To evaluate the DOX-loading efficiency, the supernatant and washed solutions were collected and the residual DOX content (R_{DOX}) was obtained by UV-vis measurement at a wavelength of 480 nm. The loading efficiency of DOX can be calculated as follows: $[(O_{DOX} - R_{DOX})/O_{DOX}] \times 100\%$, in which O_{DOX} is the original DOX content.

In vitro cytotoxicity of DOX-MUCNCs@SNTs against HeLa cells

HeLa cells were plated out in 96-well plates at a density of 8000 cells per well and were allowed to attach and grow for 24 h to allow the cells to attach. The free DOX, DOX-MUCNCs@SNTs, and MUCNCs@SNTs were added to the medium, and the cells were incubated in 5% CO_2 at 37 °C for 24 h. The concentrations of DOX were 1.5625, 3.125, 6.25, 12.5, 25, 50 μg mL^{-1} respectively and the correlative concentrations of SNTs were 17.1875, 34.375, 68.75, 137.5, 275, 550 μg mL^{-1}, respectively. Before removing the media in the tubular composites, 20 μL of MTT solution was added into each cell and incubated for another 4 h. The supernatant in each well was aspirated and 150 μL of DMSO was added to each well before the plate was examined using a microplate reader (Therom Multiskan MK3) at the wavelength of 490 nm.

Cellular uptake of the MUCNCs@SNTs

MUCNCs@SNTs composite materials were ultrasonically treated before cellular uptake and modality imaging. Cellular uptake by HeLa cells was examined using flow cytometry. FITC-labeled MUCNCs@SNTs were synthesized firstly. 2 mg FITC and 45 μL APTMS were dissolved in 1 mL ethanol and stirred at room temperature for 12 h in the dark. Then 20 μL above solution and 20 mg SNTs were added into 20 mL ethanol, and the mixture was refluxed at 80 °C for another 12 h. The composites were separated by centrifugation, washed with ethanol and dialysis against water (cutoff molecular weight: 8000–10 000 Da). For flow cytometry studies, HeLa cells (1×10^6) were seeded in 6-well culture plates and grown overnight. The cells were then treated with FITC-labeled MUCNCs@SNTs at 37 °C for 30 min and 6 h. A single cell suspension was prepared consecutively by trypsinization, washing with PBS, and filtration through 35 mm nylon mesh. Thereafter, the cells were lifted using a cell stripper (Media Tech. Inc.), and analyzed using a FACSCalibur flow cytometer (BD Biosciences) for FITC. The excitation wavelength and emission wavelength were 488 nm and 525 nm, respectively.

MR imaging of the MUCNCs@SNTs

The T_1-weighted MR images were obtained using a 0.55 T MRI magnet (Shanghai Niumag Corporation Ration NM120-Analyst). Dilutions of MUCNCs@SNTs (Gd concentration: 0.025, 0.125, 0.25, 0.5, 1 mM) in deionized water were placed in a series of 2 mL tubes for T_1-weighted MR imaging. The following parameters were adopted: TR/TE (repetition time/echo time) = 500/12 ms, FOV (field of view in cm) = 100 × 100, slice thickness = 4.9 mm.

UC luminescence imaging of the UCNCs@SNTs

The instrument of up-conversion luminescence microscopy (UCLM) was rebuilt on an inverted florescence microscope (Nikon Ti-S), an infrared laser excited unit (FF735-Di01-25 × 36, Nikon) and laser diode driver (KS3-11312-312, BWT). UC luminescence (UCL) bioimaging of HeLa (5×10^4/well) were seeded in 6-well culture plates (a clean cover slip was put in each well) and grown overnight as a monolayer, and were incubated with DOX-MUCNCs@SNTs at 37 °C for 4 h. Thereafter, the cells were washed with PBS three times, fixed with 2.5% formaldehyde at 37 °C for 10 min, and then washed with PBS three times again. UCLM imaging was performed with the reconstructive Nikon Ti–S. Cells were excited by infrared laser at 980 nm (BWT Beijing LTD, China) with output power of 250 mW.

Characterization

The X-ray diffraction (XRD) patterns of the samples were carried out on a D8 Focus diffractometer (Bruker) with use of Cu-Kα radiation (λ = 0.15405 nm). The UV-vis adsorption spectral values were measured on a U-3310 spectrophotometer. The morphology of the samples was inspected using a field emission scanning electron microscope (Philips XL 30). Transmission electron microscopy (TEM) micrograph was obtained from a FEI Tecnai G2 S-Twin transmission electron microscope with a field emission gun operating at 200 kV.

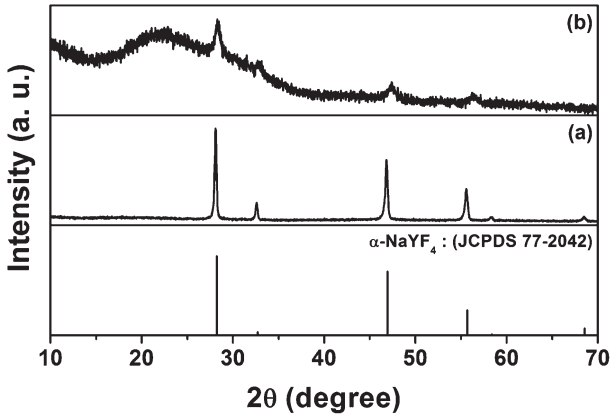

Fig. 1 XRD patterns of the PEI coated α-$NaYF_4$:Yb/Er/Gd NCs (a) and $NaYF_4$:Yb/Er/Gd@SiO_2 nanocomposites (b), as well as the JCPDS cards for $NaYF_4$, respectively.

Nitrogen adsorption/desorption analysis was measured using a Micromeritics ASAP 2020 M apparatus. The specific surface area was determined by the Brunauer-Emmett-Teller (BET) method using the data between 0.05 and 0.35. The pore volume was obtained from the *t*-plot method. The UC emission spectra were obtained using a 980 nm laser diode as the excitation source and the emission spectra were dispersed by the emission monochromator of the Acton SpectraPro-2758 equipped with R928 PMT, and the data were recorded from 400 to 700 nm. The photos of up-conversion luminescence were obtained digitally on a Nikon multiple CCD camera (DS-Ri1). A flow cytometry (FCM, BD Biosciences) with an excitation wavelength of 488 nm was used to quantify the transfection efficiency of each sample.

Results and discussion

Structure, morphology and formation of the nanocomposites

Fig. 1 shows the XRD patterns of the as-synthesized $NaYF_4$:Yb/Er/Gd and $NaYF_4$:Yb/Er/Gd@SiO_2 nanocomposites, as well as the JCPDS cards for $NaYF_4$, respectively. In Fig. 1a for samples obtained by the hydrothermal method, all the diffraction peaks can be indexed as a pure cubic α-phase of $NaYF_4$, which agrees well with the reference values (JCPDS No. 77-2042). When the electrospun precursor samples are calcined at 600 °C, a broad peak centered at $2\theta = 22^\circ$ can be observed due to the characteristic reflection from amorphous SiO_2 (JCPDS No. 29-0085). The other sharp diffraction peaks are in good agreement with those of cubic α-phase structure known from bulk α-$NaYF_4$ phase (JCPDS No. 77-2042) as shown in Fig. 1b.

Fig. 2a shows the TEM image of the $NaYF_4$ NCs co-doped with 17% Yb^{3+}, 3% Er^{3+} and 8% Gd^{3+} using PEI as a surfactant, and it can be seen that the NCs exhibit spherical shape with an average size about 30 nm. The corresponding HR-TEM (Fig. 2b) image clearly shows lattice fringes with interplanar spacing of 0.315 nm ascribed to the (111) plane of α-$NaYF_4$. PEI contains a large number of amino groups in the long molecular chain, which are capable of binding to the

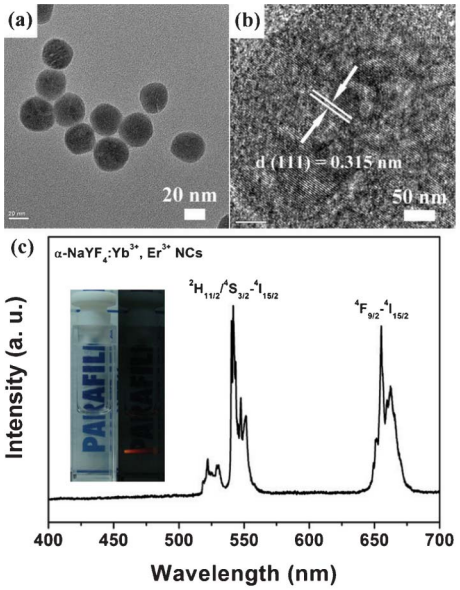

Fig. 2 TEM (a) and HR-TEM (b) images of PEI coated α- $NaYF_4$:Yb/Er/Gd NCs, UC emission spectrum and luminescent photograph of the NCs (c).

nanocrystal surface more tightly and thus it is more efficient to control the particle growth and stabilize the particles against aggregation (Fig. S1a, ESI†).[51] As can be seen in Fig. S1b, ESI†, without the addition of PEI, NCs with irregular shape and nonuniform size were produced. The UC emission spectrum and luminescent photograph of the as-synthesized α-$NaYF_4$:Yb/Er/Gd NCs are shown in Fig. 2c. In the emission spectrum for α-$NaYF_4$:Yb/Er/Gd NCs, the spectral peaks can be observed corresponding to the electron transitions of Er^{3+} ions: $^2H_{11/2}/^4S_{3/2} \rightarrow {}^4I_{15/2}$ (from 510 to 575 nm), $^4H_{9/2} \rightarrow {}^4I_{15/2}$ (660 and 675 nm),[52,53] whose emission peaks are similar to those observed in previous study for the pure UC crystals.[54] The insets of Fig. 2c give the digital photograph of α-$NaYF_4$:Yb^{3+}, Er^{3+} NCs dispersed in ethanol and the corresponding luminescent photograph under 980 nm NIR laser excitation. The results demonstrate the as-synthesized α-$NaYF_4$:Yb/Er/Gd NCs (MUCNCs) can be well dispersed in above solution and emit red light.

The morphology and structure of the electrospun precursor samples and $NaYF_4$:Yb/Er/Gd@SiO_2 nanocomposites were investigated by SEM and TEM observations. Fig. 3 shows the

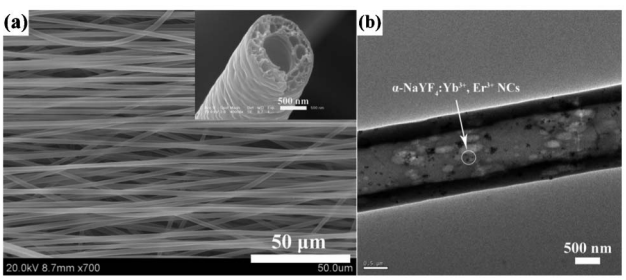

Fig. 3 SEM (a) and TEM (b) images of as-synthesis MUCNCs@precursor fibers.

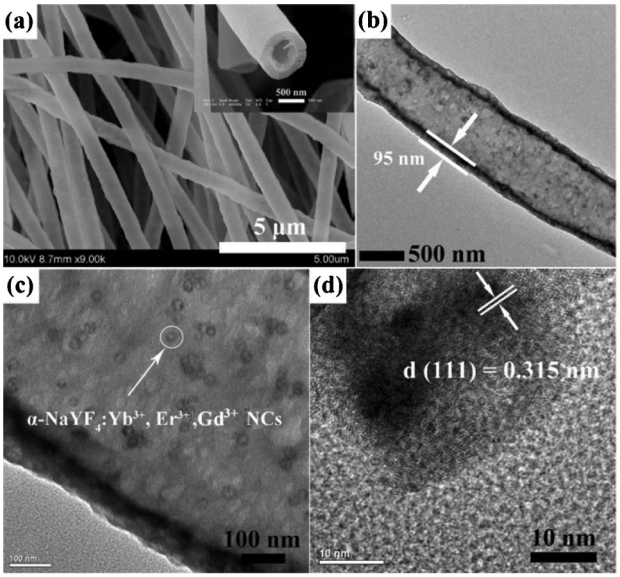

Fig. 4 SEM (a), TEM (b, c) and HR-TEM (d) images of 600 °C annealing derived MUCNCs@SiO_2 nanotubes.

SEM (a) and TEM (b) micrographs of as-prepared electrospun precursor samples. It can be found that a hollow structure had already formed within the samples after drying. The MUCNCs are dispersed uniformly in the hollow fibers. The typical average diameter of the hollow fibers is about 1.5 μm with a rough outer and inner surface as seen in the inset of Fig. 3a. The rough inner wall might be caused by the rapid phase separation during the electrospinning process. The length of these hollow fibers can reach up to the millimeter scale, which is similar to the silica fibers prepared by electrospinning with TEOS sol–gel.[55,56] In order to remove the PVP and obtain pure SNTs, the dried composite hollow fibers were calcined in air at 600 °C for 3 h. As shown in the SEM image (Fig. 4a), the outer diameter of the hollow fibers decreases to about one half of that of the precursor fibers. This reduction of the fiber diameters might be attributed to two aspects. First, PVP was completely decomposed during the high temperature annealing treatment, leaving many vacancies in the tube walls, accordingly resulting in the shrinkage of the tubes during 600 °C calcination process. On the other hand, silica molecules and MUCNCs could reconfigure in the tube walls at high temperature, which not only led to the rough surfaces of the tubes, but also to the shrinkage of the tubes. It can be clearly seen that the electrospun samples are comprised of tubular fibers with wall thickness of 75–150 nm and the outer diameters of the products range from 500 nm to 1 μm. The morphology of the MUCNCs@SNTs is further characterized by TEM and HR-TEM techniques. The tubular morphology can be clearly seen from the result of TEM due to the different electron penetrability for the edge and middle of the tubes, and the wall thickness is about 95 nm as shown in Fig. 4b. From the high-magnification of TEM image (Fig. 4c), it can be seen that α-$NaYF_4$:Yb/Er/Gd NCs also disperse uniformly in the MUCNCs@SNTs after calcination. Moreover, the obvious lattice fringes in the HR-TEM image (in Fig. 4d) confirm the high crystallinity of α-$NaYF_4$:Yb/Er/Gd NCs in the SNTs after high temperature annealing. The distance of 0.315 nm between the adjacent lattice fringes of MUCNCs@SNTs is well consistent with the d_{111} spacing (0.315 nm) of the cubic α-$NaYF_4$ (JCPDS No. 77-2042).

The possible formation process of the MUCNCs@SNTs is schematically shown in Fig. 5. The as-synthesized 30 nm-sized UCNCs coated with PEI are typically dispersible in various solvents including water, ethanol, dimethylformamide, dimethylsulphoxide and ethylene glycol which can be conducted in the electrospinning experiment directly. To illuminate the formation of tubular morphology in a polymer-solvent system, theoretical analysis and simulations have been contributed by Dayal and Kyu.[57] The fiber morphologies have been well demonstrated in terms of the phase diagram of the polymer solution, which in a manner depends on the competition between the phase separation dynamics and the evaporation rate of solvent.[58] During the electrospinning process, once the fibers were spun out from the nozzle, the ethanol solvent will evaporate rapidly from the fibers. Then, PVP would be forced to emigrate from the core of the fibers to the outer surface due to its incompatibility with TEOS. Accordingly, the TEOS-(PVP/silica) containing MUCNCs core-shell composite nanofibers were obtained (TEOS as the core and PVP/silica composite as the shell). On the other hand, TEOS is a volatile liquid, which might evaporate through the walls of the nanotubes easily. Accordingly, PVP/silica Fig. 3a),

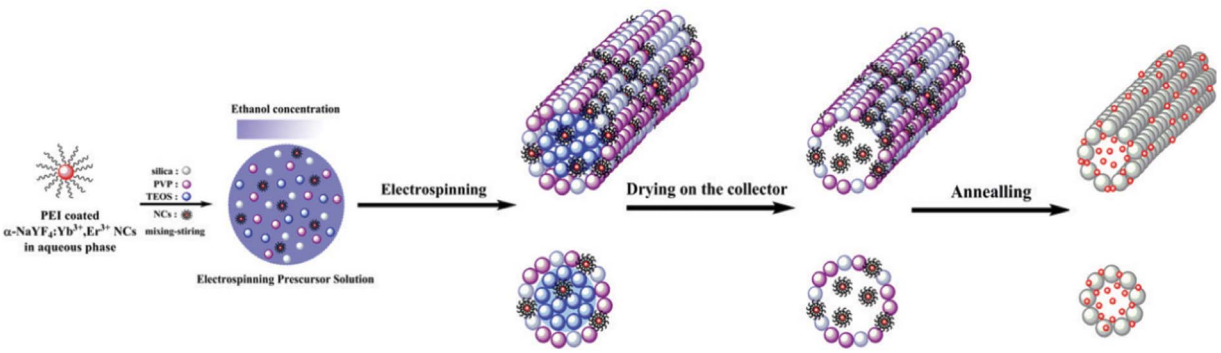

Fig. 5 Schematic diagram of the formation mechanism of SiO_2 nanotubes. Silica, grey; TEOS, blue; PVP, red. The ethanol concentration decreases from blue to white.

and the roughness of the wall is evidence of rapid phase separation during the electrospinning process, which is similar to the formation of nanoporous nanofibers. After annealing at a temperature above 600 °C, PVP molecules would be decomposed and removed completely from the composite nanotubes and MUCNCs could reconfigure in the tube walls.

In the work, we can confirm the entire removal of PVP by FT-IR. The FT-IR spectra of MUCNCs@precursor fibers (a) and pure MUCNCs@SNTs (b) are shown in Fig. S2, ESI†, respectively. In Fig. S2a, ESI†, for the as-formed precursor samples, the FT-IR spectrum shows the –OH group (3425 cm^{-1}), $-CH_2$ group (2957, 1475 and 1423 cm^{-1}), C=O group (1658 cm^{-1}), carbonates COO^- group (1384 cm^{-1}), and tertiary amine group (1291 cm^{-1}), which arise from the starting materials (ethanol, TEOS, and PVP). As shown in Fig. S2b, ESI†, for as-prepared MUCNCs@SNTs, the FT-IR spectrum presents the –OH group (3440 cm^{-1}), H_2O (1630 cm^{-1}), Si–O–Si group (ν_s, 1090 cm^{-1}; ν_{as}, 808 cm^{-1}), Si–OH group (ν_s, 957 cm^{-1}), Si–O group (δ, 465 cm^{-1}) (where ν_s represents symmetric stretching, ν_{as} represents asymmetric stretching, δ represents δ bending).[61] The MUCNCs@SNTs after calcination at 600 °C for 3 h in air will lose the majority of silanol and absorbed water, thus hydrophobic interaction between Si–O–Si and DOX may play a more important role in the adsorption of DOX. The respective N_2 adsorption/desorption isotherms of MUCNCs@SNTs are shown in Fig. S3, ESI†. It can be seen that the silica samples show similar IV isotherms and the typical H_1-hysteresis loops, demonstrating the typical tube structure. For the MUCNCs@SNTs, the BET surface area is about 601.9 $m^2\ g^{-1}$, pore volume is about 0.753 $cm^3\ g^{-1}$, and average pore size is about 5 nm.

The UC emission spectrum and UC mechanisms of the as-prepared MUCNCs@SNTs are shown in Fig. S4, ESI†, respectively. Under 980 nm NIR laser excitation, two obvious strong emission bands centered at 656 nm and 673 nm can be assigned to $^4F_{9/2} \rightarrow {}^4I_{15/2}$ transitions of Er^{3+} in the emission spectra for MUCNCs@SNTs (Fig. S4a, ESI†). The up-conversion spectrum is subject to the surface properties of Gd-doped $NaYF_4$:Yb/Er, and the presence of –OH groups and photonic band gaps in the MUCNCs@SNTs result in the quenching of green emission and enhancement of red emission.[59–61] C. H. Yan reported a novel UC photonic crystal fabricated by embedding $NaYF_4$:Yb/Er nanoparticles in inverse opals, and manipulates the UC emission behavior.[59] A relatively intense red emission was observed, while the intensity of green emission decreased sharply.[62,63] The same reason may hold for the current MUCNCs@SNTs to some extent. The UC mechanisms in Yb^{3+} and Er^{3+} co-doped materials are well investigated.[26] Initially, Yb^{3+} ions are excited from $^2F_{7/2}$ to $^2F_{5/2}$ level by 980 nm laser, and then an excited Yb^{3+} transfer its energy to Er^{3+} ($^4I_{11/2}$). Just as the electron stays on the $^4I_{11/2}$ level, a second 980 nm photon excites Yb^{3+} ions, and then the energy is transferred to Er^{3+}, resulting in the electron population on higher $^4F_{7/2}$ energetic state of the Er^{3+} ions. The Er^{3+} ion can then relax nonradiatively by a multi-phonon relaxation process to the $^2H_{11/2}$ and $^4S_{3/2}$ levels and the dominant green $^2H_{11/2} \rightarrow {}^4I_{15/2}$ and $^4S_{3/2} \rightarrow {}^4I_{15/2}$ emissions occur. Alternatively, the electron can further relax and populate the $^4F_{9/2}$ level resulting in the occurrence of red $^4F_{9/2} \rightarrow {}^4I_{15/2}$ emission. The above excitation, energy transfer and up-conversion emission process is schematically shown in Fig. S4b, ESI†.

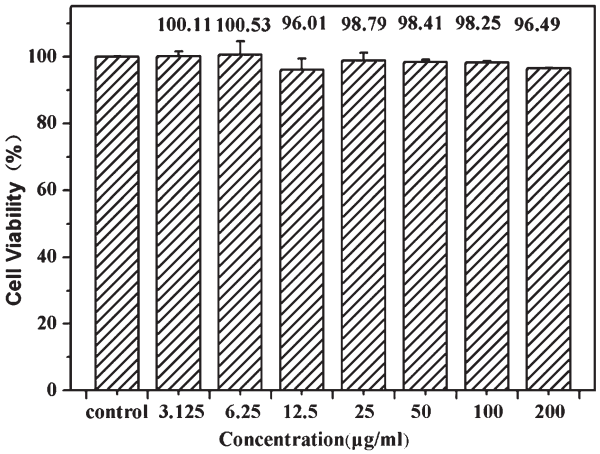

Fig. 6 The L929 fibroblast cells viability after incubating with MUCNCs@SNTs for 24 h and quantitative assays by standard MTT method.

The biocompatibility of the MUCNCs@SNTs

It is important to evaluate the biocompatibility of the carrier materials for their potential biomedical applications. The lanthanides-based UC luminescent materials have been reported to exhibit no or low cytotoxicity *in vivo* in some literatures.[64–68] Here MTT assays were performed on L929 cell lines to evaluate the cytotoxicity of our samples. As shown in Fig. 6, MUCNCs@SNTs showed no significant cytotoxic effect on the L929 cells at 3.125–200 μg mL^{-1} after incubation for 24 h. The cell viability can even reach 96.49% with the concentration as high as 200 μg mL^{-1}. The results above demonstrate that our samples have good biocompatibility and have potential to be used as drug carrier materials.

Drug loading and release properties of UCNCs@SNTs

We further examined the drug loading and release ability of as-prepared MUCNCs@SNTs. Doxorubicin hydrochloride (DOX), an anti-cancer drug, was used as a model drug to evaluate the loading and controlled release behaviors of the tubular composite samples. The actual loading level of DOX in the nanotubes is calculated to be 8.36% in weight, which is determined by the characteristic DOX optical absorbance at 480 nm. Fig. 7 gives cumulative drug release profiles for the DOX-MUCNCs@SNTs DDS in two different pH value phosphoric acidic buffer solutions (PBS) over a time period of 60 h at 37 °C. The initial burst release may be attributed to the DOX weakly adsorbed on the outer surface of the silica nanotubes, and the slow release of the rest of the DOX can be ascribed to the strong interaction between DOX molecules and the silica nanotube inner surface. Only 56.2% of the DOX is released from the SNTs even after 60 h at pH = 7.4. In contrast, almost 90% of the DOX is released in mildly acidic conditions (pH = 5.0). The drug release behavior shows that the liberation of DOX from MUCNCs@SNTs is pH-dependent. The surface zeta-

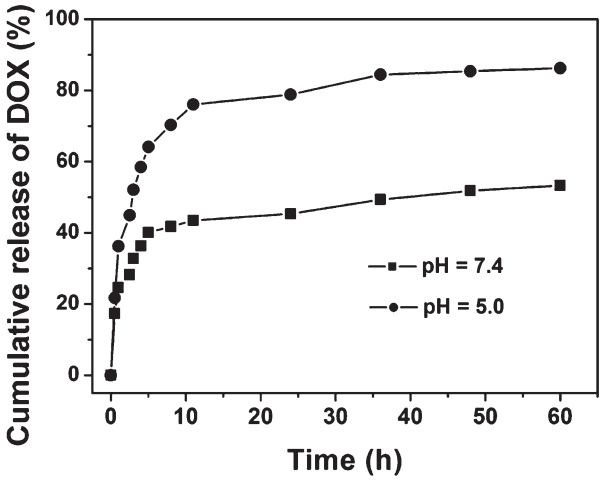

Fig. 7 Cumulative DOX release from MUCNCs@SNTs at pH = 7.4 (a) and pH = 5.0 (b).

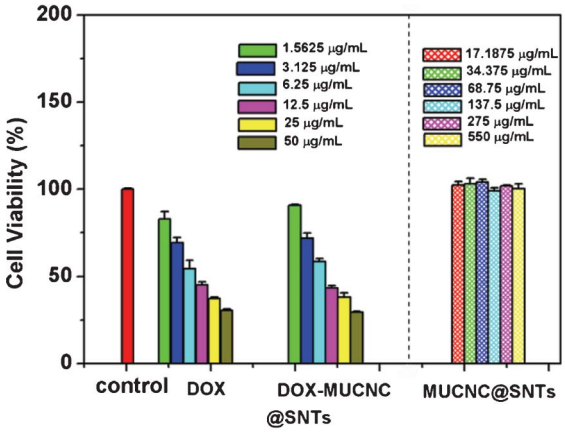

Fig. 8 *In vitro* HeLa cell viabilities after incubation 24 h with free DOX, DOX-UCNCs@SNTs and pure UCNCs@SNTs at different concentrations.

potential of the SiO_2 sample becomes more positive with the decrease of the pH value, and the weakened electrostatic adsorption force with positive charged DOX molecules results in the faster drug release at low pH values.[64,65] It is well known that the extracellular pH of many solid tumors is lower than normal tissues and presents an acidic microenvironment.[66,67] As an improvement of our former work,[43] SNTs have a larger BET surface area compared with porous silica fibers, and the N_2 adsorption/desorption isotherms demonstrate the SNTs possess cavity within the silica fiber. The tubular structure can not only hold for drugs but also release more DOX than the porous fiber structure in the same pH values PBS due to the weak electrostatic adhesion between DOX and cavity. The pH-sensitive DOX release might be beneficial at the reduced pH values in intracellular lysosomes, endosomes and certain cancerous tissues for targeted release and controlled therapy at the pathological sites.[68]

In vitro cytotoxicity effect on cancer cells

To test the pharmacological activity of the DOX-loaded nanotubes, the cytotoxic effect of DOX-loaded MUCNCs@SNTs on HeLa cells is evaluated *in vitro via* MTT assay. Fig. 8 shows the cancer cell viabilities against free DOX, DOX-MUCNCs@SNTs, and MUCNCs@SNTs for 24 h at different concentrations. The concentration of MUCNCs@SNTs was set at the same level as the MUCNCs@SNTs concentration used in the DOX-MUCNCs@SNTs. The pure MUCNCs@SNTs without DOX have no obvious cytotoxic effect on cancer cells even after 24 h of treatment with the samples at the concentration as high as 50 μg mL^{-1}. In contrast, both free DOX and DOX-MUCNCs@SNTs exhibited an increasing inhibition against HeLa cells with an increased concentration. It is found that the DOX-MUCNCs@SNTs exhibit the similar cytotoxicity to that of free DOX. Free DOX spread faster than the DOX-MUCNCs@SNTs by cellular uptake. When the concentration is higher, more DOX-MUCNCs@SNTs would be endocytosed to enter the cancer cells and release DOX inside to introduce cell death. Therefore, we conclude that MUCNCs@SNTs have potential to be used as a carrier for anti-cancer drugs.

Cellular uptake and *in vitro* MR and UCL imaging of MUCNCs@SNTs

MUCNCs@SNTs were ultrasonically treated before drug loading and cellular uptake, and the TEM image of tubular fragments were shown in Fig. S5, ESI†. From the TEM image, it can be seen that the length and diameter of fragments range from 1.5 μm to 3 μm and from 500 nm to 1 μm, respectively. Thus, we know that the ultrasonication can cut the long tubes (several hundred micrometers) into short ones effectively.

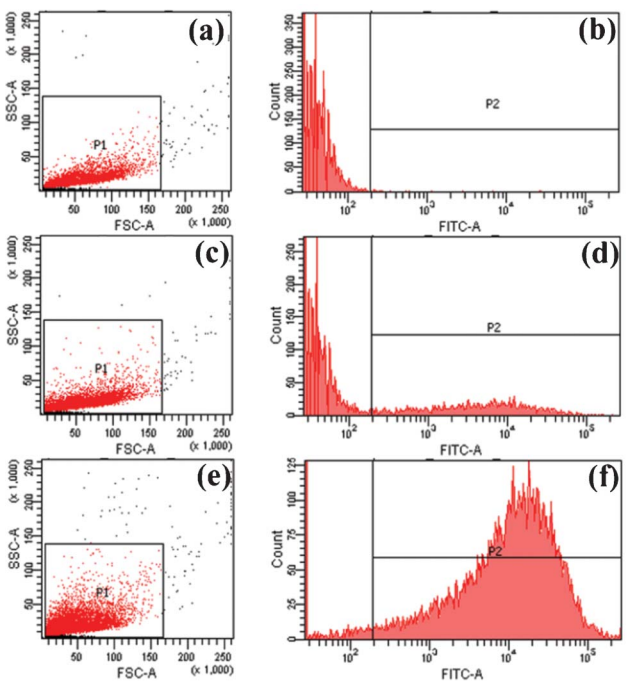

Fig. 9 Flow cytometry analysis of the control cells (a, b) and HeLa cells incubated with FITC-MUCNCs@SNTs for 30 min (c, d) and 6 h (e, f).

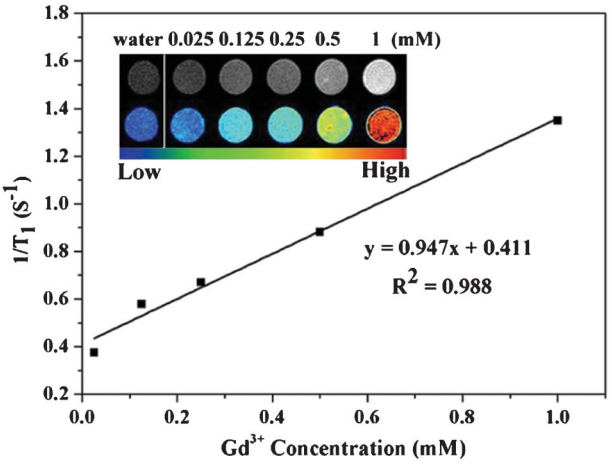

Fig. 10 Plot of R_1 ($1/T_1$, s^{-1}) *versus* Gd^{3+} concentration (1, 0.5, 0.25, 0.125, 0.025 mM of Gd^{3+}). The slope indicates the specific relaxivity. Inset: the T_1-weighted and color-mapped MR images of MUCNCs@SNTs with deionized water (0 mM) as the reference.

Since MUCNCs@SNTs were labeled with fluorescent dye, FITC, the cell uptake degree of the composites could be quantified with flow cytometry by determining the red fluorescence emitted from FITC-MUCNCs@SNTs treated HeLa cells. After incubation with the samples for different lengths of time (30 min, and 6 h), the cell-labeling ability of composites was estimated by flow cytometry. As revealed by Fig. 9, FITC-MUCNCs@SNTs were taken up by HeLa cells compared to the controlled cells, and the cellular uptake of samples increase with incubation time.

To evaluate the MR properties of MUCNCs@SNTs, an *in vitro* T_1-weighted MR imaging for MUCNCs@SNTs was conducted on a Shanghai Niumag Corporation Ration NM120-Analyst system. As shown in Fig. 10, the slope of the plot of $1/T_1$ *versus* the Gd^{3+} concentration, the ionic longitudinal relaxivity (R_1) was determined to be 0.947 s^{-1} mM^{-1}. With the increase of Gd^{3+} concentration, the T_1-weighted MRI resulted in brighter images (inset of Fig. 11). To obtain a clear view of the dose-dependent positive enhancement effect, colored T_1-weighted MR images are also presented (inset of Fig. 11). As the concentration increasing, the color of the MR images changed from blue to red, corresponding to the signal from low to high level. The results above demonstrated that the composites could serve as a T_1-MRI contrast agent. The interaction of HeLa cells with the MUCNCs@SNTs was also investigated by up-conversion luminescent microscopy (UCLM) equipped with infrared laser excitation at 980 nm. HeLa cells were incubated with MUCNCs@SNTs (100 μg mL^{-1}) at 37 °C for 4 h for cell imaging (Fig. 11). Bright-field measurements after treatment with the UCNCs@SNTs confirmed that the cells are viable throughout the imaging experiments (Fig. 11a). Moreover, the red UC luminescent signal can be observed from the HeLa cells under laser excitation at 980 nm (Fig. 11b). Overlays of bright-field and UC luminescent images further demonstrate that the luminescence is evident in the intracellular region (Fig. 11c). This indicates that MUCNC@SNTs penetrate the cell membrane of HeLa cells, and confirms that MUCNC@SNTs are promising candidates for use as bioimaging probes.

Conclusions

In summary, water-dispersible magnetic and up-conversion luminescent $NaYF_4$:Yb/Er/Gd NCs were synthesized by a hydrothermal route using PEI as an organic polymer surfactant. Then MUCNCs@precursor fibers were prepared by electrospinning using precursor solution containing MUCNCs. Finally, MUCNCs@SNTs were obtained after high temperature annealing (600 °C), resulting in the formation of magnetic/UC luminescent hollow silica fibers. The as-prepared MUCNCs@SNTs show the attractive properties of regular tubular morphology, good biocompatibility and high effectiveness of drug release which are suitable for anti-cancer drug (DOX) storage/release as a drug carrier. It is found that the liberation of DOX from MUCNCs@SNTs has a pH-sensitive release pattern. DOX is shuttled into cells by MUCNCs@SNTs carriers and released inside cells after endocytosis, and the DOX-MUCNCs@SNTs exhibits similar cytotoxicity to free DOX. We also prove that the applications of MUCNCs@SNTs for UCL and MRI multimodality *in vitro* imaging can be

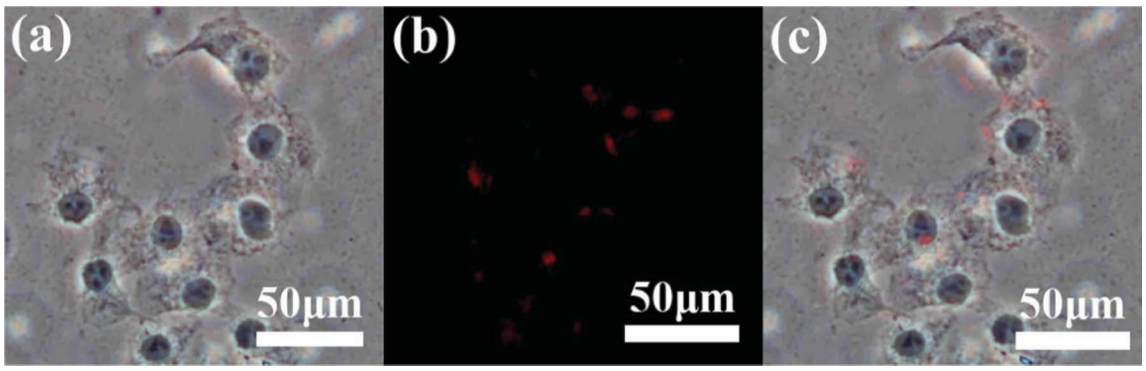

Fig. 11 Inverted florescence microscope images of HeLa cells incubated with UCNCs@SNTs, bright-field image (a), UC luminescent image (b) and the overlay of bright-field and UC luminescent images (c).

established successfully. These studies indicate that electrospinning is a facile and novel route for the preparation of functionalized silica nanotube materials, which have potential applications in the fields of drug delivery and multimodality imaging based on their bioactive, magnetic, luminescent and hollow properties.

Acknowledgements

This project is financially supported by National Basic Research Program of China (2010CB327704), National High Technology Program of China (2011AA03A407), the National Natural Science Foundation of China (NSFC 51202239, 51172228, 21101149, 51172227, 21221061), and Science and Technology Development Program of Jilin Province for Youths (20100106).

Notes and references

1 M. A. C. Stuart, W. T. S. Huck, J. Genzer, M. Mueller, C. Ober, M. Stamm, G. B. Sukhorukov, I. Szleifer, V. V. Tsukruk, M. Urban, F. Winnik, S. Zauscher, I. Luzinov and S. Minko, *Nat. Mater.*, 2010, **9**, 101–113.
2 Z. Wu, K. Chen, I. Yildiz, A. Dirksen, R. Fischer, P. E. Dawson and N. F. Steinmetz, *Nanoscale*, 2012, **4**, 3567–3576.
3 M. Look, A. Bandyopadhyay, J. S. Blum and T. M. Fahmy, *Adv. Drug Delivery Rev.*, 2010, **62**, 378–393.
4 X. Guo and F. C. Szoka, *Acc. Chem. Res.*, 2003, **36**, 335–341.
5 L. Rajendran, H.-J. Knoelker and K. Simons, *Nat. Rev. Drug Discovery*, 2010, **9**, 29–42.
6 J. H. Huang, T. C. Lai, L. C. Cheng, R. S. Liu, C. H. Lee, M. Hsiao, C. H. Chen, L. J. Her and D. P. Tsai, *J. Mater. Chem.*, 2011, **21**, 14821–14829.
7 Y. Liu, D. Tu, Z. Chen, M. Huang, H. Zhu, E. Ma and X. Chen, *Nanoscale*, 2013, **5**, 1369–1384.
8 M. A. Rauschmann, T. A. Wichelhaus, V. Stirnal, E. Dingeldein, L. Zichner, R. Schnettler and V. Alt, *Biomaterials*, 2005, **26**, 2677–2684.
9 F. Chen, P. Huang, Y.-J. Zhu, J. Wu, C.-L. Zhang and D.-X. Cui, *Biomaterials*, 2011, **32**, 9031–9039.
10 M. P. Ginebra, T. Traykova and J. A. Planell, *J. Controlled Release*, 2006, **113**, 102–110.
11 M. Julien, I. Khairoun, R. Z. LeGeros, S. Delplace, P. Pilet, P. Weiss, G. Daculsi, J. M. Bouler and J. Guicheux, *Biomaterials*, 2007, **28**, 956–965.
12 X. Yan, C. Yu, X. Zhou, J. Tang and D. Zhao, *Angew. Chem., Int. Ed.*, 2004, **43**, 5980–5984.
13 A. Lopez-Noriega, D. Arcos, I. Izquierdo-Barba, Y. Sakamoto, O. Terasaki and M. Vallet-Regi, *Chem. Mater.*, 2006, **18**, 3137–3144.
14 Y. Hong, X. Chen, X. Jing, H. Fan, B. Guo, Z. Gu and X. Zhang, *Adv. Mater.*, 2010, **22**, 754–758.
15 L. L. Hench and J. M. Polak, *Science*, 2002, **295**, 1014–1017.
16 L. Ji, G. Jell, Y. Dong, J. R. Jones and M. M. Stevens, *Chem. Commun.*, 2011, **47**, 9048–9050.
17 T. Lopez, K. Espinoza, A. Kozina, A. Galano and R. Alexander-Katz, *J. Phys. Chem. C*, 2010, **114**, 20022–20027.
18 C. Wu, J. Chang and W. Fan, *J. Mater. Chem.*, 2012, **22**, 16801–16809.
19 B. M. Barth, E. I. Altinoglu, S. S. Shanmugavelandy, J. M. Kaiser, D. Crespo-Gonzalez, N. A. DiVittore, C. McGovern, T. M. Goff, N. R. Keasey, J. H. Adair, T. P. Loughran Jr., D. F. Claxton and M. Kester, *ACS Nano*, 2011, **5**, 5325–5337.
20 S. J. Son, X. Bai and S. B. Lee, *Drug Discovery Today*, 2007, **12**, 650–656.
21 R. Tenne, *Nat. Nanotechnol.*, 2006, **1**, 103–111.
22 L. Li, F. Tang, H. Liu, T. Liu, N. Hao, D. Chen, X. Teng and J. He, *ACS Nano*, 2010, **4**, 6874–6882.
23 J. H. Jung, M. Park and S. Shinkai, *Chem. Soc. Rev.*, 2010, **39**, 4286–4302.
24 Q. Ju, D. Tu, Y. Liu, R. Li, H. Zhu, J. Chen, Z. Chen, M. Huang and X. Chen, *J. Am. Chem. Soc.*, 2012, **134**, 1323–1330.
25 D. Li and Y. Xia, *Adv. Mater.*, 2004, **16**, 1151–1170.
26 H. Hu, M. Yu, F. Li, Z. Chen, X. Gao, L. Xiong and C. Huang, *Chem. Mater.*, 2008, **20**, 7003–7009.
27 Y. Liu, D. Tu, H. Zhu, R. Li, W. Luo and X. Chen, *Adv. Mater.*, 2010, **22**, 3266–3271.
28 C. Zhang, H.-P. Zhou, L.-Y. Liao, W. Feng, W. Sun, Z.-X. Li, C.-H. Xu, C.-J. Fang, L.-D. Sun, Y.-W. Zhang and C.-H. Yan, *Adv. Mater.*, 2010, **22**, 633–637.
29 F. Wang, Y. Han, C. S. Lim, Y. Lu, J. Wang, J. Xu, H. Chen, C. Zhang, M. Hong and X. Liu, *Nature*, 2010, **463**, 1061–1065.
30 F. Wang, D. Banerjee, Y. Liu, X. Chen and X. Liu, *Analyst*, 2010, **135**, 1839–1854.
31 A. K. Sharma, K. H. Son, B. Y. Han and K.-S. Sohn, *Adv. Funct. Mater.*, 2010, **20**, 1750–1755.
32 C. C. Lin and R. S. Liu, *J. Phys. Chem. Lett.*, 2011, **2**, 1268–1277.
33 W. Luo, C. Fu, R. Li, Y. Liu, H. Zhu and X. Chen, *Small*, 2011, **7**, 3046–3056.
34 T. Cao, Y. Yang, Y. Gao, J. Zhou, Z. Li and F. Li, *Biomaterials*, 2011, **32**, 2959–2968.
35 C.-J. Wang, L.-H. Weng, J.-Y. Ko, Y.-C. Sun, Y.-J. Yang and F.-S. Wang, *Arch. Orthop. Trauma Surg.*, 2011, **131**, 1153–1158.
36 N. F. Idris, J. C. Neill and C. H. Large, *Frontiers in Behavioral Neuros.*, 2009, **3**, 1–8.
37 H. Yang and B. Wang, *Clim. Dyn.*, 2011, **38**, 655–665.
38 H. Yang, Y. Zhuang, H. Hu, X. Du, C. Zhang, X. Shi, H. Wu and S. Yang, *Adv. Funct. Mater.*, 2010, **20**, 1733–1741.
39 J. Yang, Y. Deng, Q. Wu, J. Zhou, H. Bao, Q. Li, F. Zhang, F. Li, B. Tu and D. Zhao, *Langmuir*, 2010, **26**, 8850–8856.
40 J. Zhou, Z. Liu and F. Li, *Chem. Soc. Rev.*, 2012, **41**, 1323–1349.
41 P. P. Yang, S. L. Gai and J. Lin, *Chem. Soc. Rev.*, 2012, **41**, 3679–3698.
42 Z. Hou, C. Zhang, C. Li, Z. Xu, Z. Cheng, G. Li, W. Wang, C. Peng and J. Lin, *Chem.–Eur. J.*, 2010, **16**, 14513–14519.
43 Z. Y. Hou, C. X. Li, P. A. Ma, G. G. Li, Z. Y. Cheng, C. Peng, D. M. Yang, P. P. Yang and J. Lin, *Adv. Funct. Mater.*, 2011, **21**, 2356–2365.

44 X. Kang, Z. Cheng, D. Yang, P. a. Ma, M. Shang, C. Peng, Y. Dai and J. Lin, *Adv. Funct. Mater.*, 2012, **22**, 1470–1481.
45 Y. Dai, P. a. Ma, Z. Cheng, X. Kang, X. Zhang, Z. Hou, C. Li, D. Yang, X. Zhai and J. Lin, *ACS Nano*, 2012, **6**, 3327–3338.
46 X. Zhang, P. Yang, C. Li, D. Wang, J. Xu, S. Gai and J. Lin, *Chem. Commun.*, 2011, **47**, 12143–12145.
47 D. Yang, C. Li, G. Li, M. Shang, X. Kang and J. Lin, *J. Mater. Chem.*, 2011, **21**, 5923–5927.
48 D. Tu, Y. Liu, H. Zhu, R. Li, L. Liu and X. Chen, *Angew. Chem., Int. Ed.*, 2013, **52**, 1128–1133.
49 T. He, W. Wei, L. Ma, R. Chen, S. Wu, H. Zhang, Y. Yang, J. Ma, L. Huang, G. G. Gurzadyan and H. Sun, *Small*, 2012, **8**, 2163–2168.
50 F. Wang, D. K. Chatterjee, Z. Li, Y. Zhang, X. Fan and M. Wang, *Nanotechnology*, 2006, **17**, 5786–5791.
51 S. Kobayashi, K. Hiroishi, M. Tokunoh and T. Saegusa, *Macromolecules*, 1987, **20**, 1496–1500.
52 X. Wang, J. Zhuang, Q. Peng and Y. D. Li, *Nature*, 2005, **437**, 121–124.
53 F. Wang and X. Liu, *Chem. Soc. Rev.*, 2009, **38**, 976–989.
54 G. S. Yi, H. C. Lu, S. Y. Zhao, G. Yue, W. J. Yang, D. P. Chen and L. H. Guo, *Nano Lett.*, 2004, **4**, 2191–2196.
55 S.-S. Choi, S. G. Lee, S. S. Im, S. H. Kim and Y. L. Joo, *J. Mater. Sci. Lett.*, 2003, **22**, 891–893.
56 C. Shao, H. Kim, J. Gong and D. Lee, *Nanotechnology*, 2002, **13**, 635.
57 P. Dayal and T. Kyu, *J. Appl. Phys.*, 2006, **100**, 043512–043516.
58 W. Wang, J. Zhou, S. Zhang, J. Song, H. Duan, M. Zhou, C. Gong, Z. Bao, B. Lu, X. Li, W. Lan and E. Xie, *J. Mater. Chem.*, 2010, **20**, 9068–9072.
59 Z.-X. Li, L.-L. Li, H.-P. Zhou, Q. Yuan, C. Chen, L.-D. Sun and C.-H. Yan, *Chem. Commun.*, 2009, 6616–6618.
60 J. Pichaandi, F. C. J. M. van Veggel and M. Raudsepp, *ACS Appl. Mater. Interfaces*, 2010, **2**, 157–164.
61 Z.-L. Wang, J. H. Hao and H. L. W. Chan, *J. Mater. Chem.*, 2010, **20**, 3178–3185.
62 S. Heer, K. Kömpe, H. U. Güdel and M. Haase, *Adv. Mater.*, 2004, **16**, 2102–2105.
63 J. F. Suyver, J. Grimm, K. W. Krämer and H. U. Güdel, *J. Lumin.*, 2005, **114**, 53–59.
64 M. Chen, S. Zhou, L. Wu, S. Xie and Y. Chen, *Macromol. Chem. Phys.*, 2005, **206**, 1896–1902.
65 S. Tang, X. Huang, X. Chen and N. Zheng, *Adv. Funct. Mater.*, 2010, **20**, 2442–2447.
66 Z. M. Bhujwalla, D. Artemov, P. Ballesteros, S. Cerdan, R. J. Gillies and M. Solaiyappan, *NMR Biomed.*, 2002, **15**, 114–119.
67 D. C. Drummond, M. Zignani and J.-C. Leroux, *Prog. Lipid Res.*, 2000, **39**, 409–460.
68 W. Wei, G.-H. Ma, G. Hu, D. Yu, T. McLeish, Z.-G. Su and Z.-Y. Shen, *J. Am. Chem. Soc.*, 2008, **130**, 15808–15810.

